Bachelor's Thesis

An accordion lattice setup for a dysprosium quantum gas microscope

Julian Bolsinger

Examiner: Prof. Dr. Tilman Pfau
Supervisor: Fiona Hellstern

Submitted to the
University of Stuttgart
5th Institute of Physics

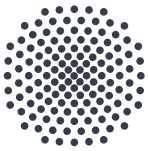

University of Stuttgart
5th Institute of Physics

August 9, 2024

Declaration of Authorship

Hiermit versichere ich gemäß § 27 Abs. 7 der Prüfungsordnung der Universität Stuttgart für den Bachelorstudiengang Physik vom 31.07.2015,

1. dass ich diese Arbeit selbständig verfasst habe,
2. dass ich keine anderen als die angegebenen Quellen benutzt und alle wörtlich oder sinngemäß aus anderen Werken übernommenen Aussagen als solche gekennzeichnet habe,
3. dass die eingereichte Arbeit weder vollständig noch in wesentlichen Teilen Gegenstand eines anderen Prüfungsverfahrens gewesen ist, und
4. dass das elektronische Exemplar mit den anderen Exemplaren übereinstimmt.

Stuttgart, den 09.09.2024 Julian Bolsinger

Abstract

Quantum gas microscopy with highly magnetic atoms such as dysprosium offers the opportunity to study dipole-dipole interactions of individual atoms. In order to capture the atoms on individual lattice sites the atoms need to be cooled, trapped and squeezed into a flat potential before they can be loaded into the science lattice. An accordion lattice is an optical lattice system that allows for continuous control over the spacing of the lattice while maintaining atom confinement. In this work a setup for such a dynamic lattice is presented that later on can be used to compress the ultracold atom cloud into an effectively two-dimensional geometry.

A laser beam with a wavelength of 1064 nm is deflected by an acousto-optical deflector and divided into two parallel beams by a pair of Dove prisms. The Dove prisms are precisely aligned and adhesively bonded together using white light interferometry. The two beams are focused by a lens so that they interfere at a shallow angle and form an optical lattice in the focal plane. Modifying the radio frequency of the acousto-optical deflector alters the distance between the two interfering beams, thereby enabling active control of the periodicity of the lattice.

Imaging of the intensity profile in the focal plane yields the expected interference patterns with a lattice spacing range between 9 µm and 76 µm. The periodicity aligns closely with the theoretical predictions over the entire radio frequency range and the central fringe moves less than 2.4 µm within this range.

Zusammenfassung

Die Quantengasmikroskopie mit hochmagnetischen Atomen wie Dysprosium bietet die Möglichkeit, Dipol-Dipol-Wechselwirkungen einzelner Atome zu untersuchen. Um die Atome auf einzelnen Gitterplätzen einfangen zu können, müssen die Atome abgekühlt, eingefangen und in ein flaches Potential gepresst werden, bevor sie in das Forschungsgitter geladen werden können. Ein Akkordeon-Gitter ist ein optisches Gittersystem, das eine kontinuierliche Kontrolle über die Gitterabstände ermöglicht und gleichzeitig die Atome einschließt. In dieser Arbeit wird ein Aufbau für ein solches dynamisches Gitter vorgestellt, das später dazu verwendet werden kann, die ultrakalte Atomwolke in eine effektiv zweidimensionale Geometrie zu komprimieren.

Ein Laserstrahl mit einer Wellenlänge von 1064 nm wird durch einen akusto-optischen Deflektor abgelenkt und durch ein Paar Dove-Prismen in zwei parallele Strahlen aufgeteilt. Die Dove-Prismen werden mit Hilfe von Weißlichtinterferometrie präzise ausgerichtet und zusammengeklebt. Die beiden Strahlen werden durch eine Linse so fokussiert, dass sie in einem flachen Winkel interferieren und in der Brennebene ein optisches Gitter bilden. Durch Änderung der Radiofrequenz des akusto-optischen Deflektors wird der Abstand zwischen den beiden interferierenden Strahlen verändert, wodurch die Periodizität des Gitters aktiv gesteuert werden kann.

Die Abbildung des Intensitätsprofils in der Fokusebene ergibt die erwarteten Interferenzmuster mit einem Gitterabstand zwischen 9 µm und 76 µm. Die Periodizität stimmt eng mit den theoretischen Vorhersagen über den gesamten Radiofrequenzbereich überein und das zentrale Intensitätsmaximum bewegt sich weniger als 2.4 µm in diesem Bereich.

Contents

List of Figures

1 Introduction

Ultracold atoms in optical lattices have emerged as a powerful platform for investigating quantum many-body physics [1]. The high level of controlability and flexibility of the system allows for modeling and simulating complex many-body quantum problems. Optical lattices are of particular interest for simulating the behavior of condensed matter systems. For instance, ultracold atoms can be used to implement a Bose-Hubbard or Fermi-Hubbard model to study condensed-matter phenomena such as superconductivity or quantum phase transitions.

A key technique for ultracold atom research is quantum gas microscopy, which enables the precise detection and manipulation of atoms [2]. High-resolution imaging techniques, combined with optical lattices, are capable of resolving atoms on individual lattice sites in two dimensions by capturing scattered photons. The two-dimensional imaging capability of quantum gas microscopy requires a two-dimensional atomic cloud in the focal plane of the microscope. Otherwise, the visibility of atoms in the focal plane would be reduced due to the limited depth of focus.

An optical lattice is created using interfering laser beams, resulting in a spatially dependent intensity that traps the atoms via the dipole force. Several methods have been realized to achieve a flat, quasi-two-dimensional cloud of cold atoms.

One method is the magnetic resonance technique, also referred to as "knifing" [3, 4]. First, a one-dimensional optical lattice is formed by retro-reflecting a laser beam, thereby creating a standing wave optical dipole trap. During the loading of ultracold atoms into the lattice, multiple layers are occupied. To capture solely the atoms situated at the focal plane, all other atoms are pushed out using a magnetic resonance. A magnetic field gradient gives rise to the splitting of magnetic sublevels of the atoms which is known as the Zeeman effect. Consequently, the resonance frequency depends on the spatial position within the lattice. By applying a microwave pulse that is resonant with specific spin states, it is possible to address individual layers. This allows the internal state of the layer in the focal plane to be flipped. A subsequent microwave pulse then pushes out the remaining atoms.

Another method is to utilize an accordion optical lattice with active control of the lattice spacing [5]. The optical lattice is formed by two laser beams that interfere at a shallow

angle, and the lattice spacing can be controlled by modifying the intersection angle. The ultracold atoms are loaded into the potential of a one-dimensional lattice with an initially large periodicity. As the lattice is compressed, the atoms are increasingly confined.

This thesis implements the accordion approach which provides a stable way to trap and compress a cloud of ultracold atoms. It is anticipated that this method will result in the lowest atom loss compared to the other methods as more atoms can be captured within the compressed layer.

Once the atoms have been cooled to quantum degeneracy, the crossed optical dipole trap is gradually turned off and a vertically adjustable accordion lattice with the largest lattice spacing is overlapped. Here, the atoms are compressed into a thin sheet, guaranteeing that they are restricted to a single layer in the final science lattice. This final science lattice confines the atoms within the x-y-plane, ensuring precise control and study of their interactions. To achieve a high transfer efficiency and match the trapping frequencies of the other lattices, a wavelength of 1064 nm is selected for the accordion lattice.

The optical lattice will be used to image quantum gases of dipolar magnetic atoms, namely ultracold dysprosium atoms. Dysprosium is a lanthanide element with a particularly large dipole moment which gives rise to long-range magnetic dipole-dipole interactions. The strongly dipolar Bose-Einstein condensate of dysprosium represents an optimal system to study complex states of matter.

2 Theory

In this chapter, the foundational concepts for this thesis will be explained, covering the basics of Gaussian optics and atom trapping.

2.1 Optics

2.1.1 Geometrical optics and wave optics

Optics can be divided into two sub-areas, namely geometrical optics and wave optics. Geometrical optics treats light as rays, i. e. in this model, light propagates in a straight line in a bundle of rays. The rays of light follow Fermat's principle, which means they always take the path with the shortest transit time between two points. Geometrical optics describes phenomena such as reflection, refraction or diffraction to a good approximation [6, 7].

In contrary, wave optics treats light as electromagnetic waves. Their behavior is described by the wave equation

$$\nabla^2 U(\vec{r},t) - \frac{1}{c^2}\frac{\partial^2 U(\vec{r},t)}{\partial t^2} = 0 \tag{2.1}$$

where $c = 299\,792\,\mathrm{km/s}$ is the speed of light in a vacuum [8]. Wave optics explains phenomena such as diffraction according to the Huygens-Fresnel principle and interference when waves are superimposed.

2.1.2 Gaussian beam optics

One of the most important types of electromagnetic waves are Gaussian beams. Gaussian beam optics is an approximation method in which light rays are viewed as waves with a Gaussian intensity profile in the transverse plane. This approach combines wave optics with geometrical optics, whereby the Gaussian rays propagating in z-direction are characterized by the intensity distribution

$$I(x,y,z) = \frac{2P}{\pi w(z)^2}\exp\left(-2\left(\frac{\rho}{w(z)}\right)^2\right). \tag{2.2}$$

Here, $\rho = \sqrt{x^2 + y^2}$ is the radial distance to the beam axis and $w(z)$ is the beam radius.

At the beam radius w, the intensity is equal to $1/e^2$ of the intensity maximum. It can be calculated using the beam propagation formula

$$w(z) = w_0 \sqrt{1 + \left(\frac{z}{z_0}\right)^2} \tag{2.3}$$

where w_0 is the radius at the beam waist – i. e. the minimum radius – and $z_0 = \frac{\pi w_0^2}{\lambda}$ is the Rayleigh length. At $z = z_0$, the beam radius is by definition $w(z_0) = \sqrt{2} w_0$, which means that the cross-sectional area of the Gaussian beam has doubled compared to the beam waist [9].

The beam divergence is determined by the opening angle

$$\theta = \arctan\left(\frac{w_0}{z_0}\right) \approx \frac{\lambda}{\pi w_0} \tag{2.4}$$

for small angles calculated from w_0 and the wavelength λ. In order to achieve a specific waist after a lens with a focal length of f, the requisite beam diameter d is determined by

$$d = 2f \tan\theta = \frac{2\lambda f}{\pi w_0}. \tag{2.5}$$

The beam characteristics are shown in figure 2.1.

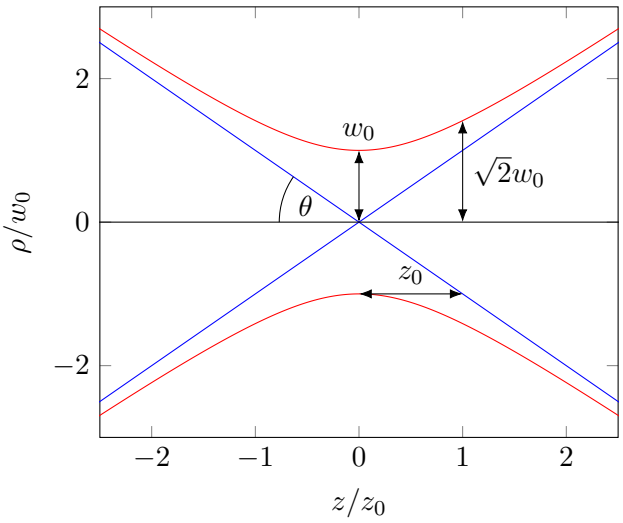

Figure 2.1: The beam radius of a Gaussian beam propagating in the z-direction follows a hyperbolic curve (——), which is characterized by the beam waist w_0 and the Rayleigh length z_0. For $z \to \pm\infty$, the beam radius can be approximated by a cone (——) with divergence angle θ.

2.1.3 Polarization

For electromagnetic waves, the direction of propagation $\vec{z}$, electric field strength vector $\vec{E}$ and magnetic field strength vector $\vec{B}$ are perpendicular to each other. However, if the direction of propagation is given, there is an unspecified degree of freedom, which is usually assigned to the direction of oscillation of the electric field vector due to its greater experimental significance.

Light is generally unpolarized, i. e. $\vec{E}$ has no preferred direction and is zero on statistical average. In the case of fully polarized light, the field vector follows a path that varies periodically over time depending on the type of polarization. In addition to fully unpolarized and fully polarized light, there are also all intermediate stages known as partial polarization. The latter can be understood as a superposition of fully polarized light and non-polarized light, whereby the proportion of polarized light corresponds to the degree of polarization [7].

If $\vec{E}$ moves on a circular path relative to the propagation – in absolute terms, the movement would follow a spiral – the wave is called circularly polarized. This type of polarization can be achieved if the x and y directions of the wave have the same amplitudes and a phase shift of $\frac{\pi}{2} \equiv \frac{\lambda}{4}$. Circularly polarized light can be further divided into right-circularly and left-circularly polarized light, depending on the direction of rotation of the $\vec{E}$ vector. A generalization of circular polarization is elliptically polarized light, in which the amplitudes are different or the phase shift is arbitrary. The field vector then describes an elliptical path relative to the direction of propagation [6].

If the electric field vector always oscillates in one direction only, the wave is called linearly polarized. The naming convention is based on its orientation relative to the plane of incidence, which contains the propagation vector and the surface normal. Special cases occur if the vector oscillates perpendicular and parallel to the plane of incidence, which is called s- and p-polarization, respectively.

The polarization state can be changed by using a waveplate; most common are $\lambda/2$- and $\lambda/4$-waveplates. Waveplates are made of birefringent materials that have different indeces of refraction along the crystal axes. As a result, the polarization components along these axes travel with different speed and built up a relative phase. For a $\lambda/2$-waveplate this phase is π, leading to a rotation of linearly polarized light depending on the orientation of the waveplate. A $\lambda/4$-waveplate shifts the relative phase by $\pi/2$, turning linear polarization into elliptical polarization.

Another optical element to influence the polarization of light is a polarizing beamsplitter cube. A beamsplitter layer running diagonally through the cube reflects the s-polarized

component of the incident beam while allowing the p-polarized component to pass through the beamsplitter unimpeded.

2.1.4 Refraction

A monochromatic wave of frequency ν travels in a medium with refractive index n_1 at phase velocity $c_1 = c/n_1$, where c is the speed of light in a vacuum. If the wave hits the interface to a medium with a refractive index n_2 at the angle of incidence α, the beam is refracted due to the different propagation speed c_2. According to Snell's law of refraction

$$\frac{\sin\alpha}{\sin\beta} = \frac{c_1}{c_2} = \frac{n_2}{n_1} \tag{2.6}$$

the angle of incidence β can be calculated from the ratio of the refractive indices or the phase velocities. As shown in figure 2.2, light rays are refracted towards the normal at the transition from the optically denser to the optically thinner medium – i. e. from medium 1 to medium 2 with $n_1 > n_2$ [6].

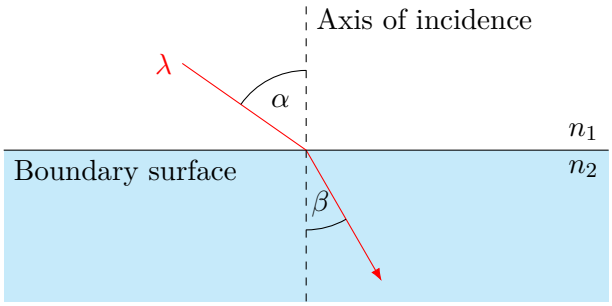

Figure 2.2: A light beam of wavelength λ is refracted at the interface of two media with different refractive indices n_1 and n_2. The angle of incidence α and angle of reflection β are measured relative to the axis of incidence.

2.1.5 Imaging equation

The ray path through a lens is generally complex, but can be greatly simplified for thin, symmetrical lenses and small distances from the optical axis. The principal plane, which is useful for constructing the optical path, lies in the center of the lens. In addition to the principal plane, the focal point or focus must be known at which rays parallel to the optical axis intersect after refraction at the lens. The distance between the principal plane and the focus is called the focal length f of a lens. For the special case of thin lenses mentioned

above, the focal length can be calculated using the imaging equation

$$\frac{1}{f} = \frac{1}{g} + \frac{1}{b} \tag{2.7}$$

from the object width g and the image width b. The object or image width is the distance between the object or screen and the principal plane [6].

2.2 Atom traps

In experiments with ultracold atoms, trapping methods are crucial for controlling the atoms. While charged particles can be cooled using the Coulomb interaction, neutral particles require a different method. Various techniques have been developed for this purpose, including magnetic traps, optical traps, and magneto-optical traps, which combine the two aforementioned approaches.

Magnetic traps are capable of trapping atoms with a magnetic dipole moment by means of inhomogeneous magnetic fields. In the presence of a magnetic field, the atomic energy levels shift due to the Zeeman effect. If an external magnetic field gradient is applied, low-field seeking atoms experience a force towards the local minima of the field.

The second type of traps are optical dipole traps. In this trap the electric field of a light beam induces an electric dipole moment in the atom. Due to the induced dipole moment the atoms experience a dipole force towards the maximum in the electric field gradient of the light. The intensity distribution of the light source acts as a potential that confines the atoms.

2.2.1 Lorentz oscillator

The optical dipole force can be derived classically from the Lorentz oscillator model [10]. In this model an electron with mass m and charge e oscillates around the atom at an eigenfrequency ω_0. It is driven by a laser with electric and magnetic fields, $\vec{E}$ and $\vec{B}$, and follows the differential equation

$$\ddot{\vec{x}} + \Gamma\dot{\vec{x}} + \omega_0^2\vec{x} = -\frac{e}{m}\vec{E}(t) - \frac{e}{m}\dot{\vec{x}} \times \vec{B}(t). \tag{2.8}$$

The variable x represents the position of the electron, while the parameter Γ denotes the damping rate. The magnetic interaction term is usually omitted because $\left|\vec{B}\right| \ll \left|\vec{E}\right|$. For a propagating wave, $\vec{E}(t) = \vec{E}(\omega)\exp(-i\omega t)$, the solution to this differential equation is that of a damped harmonic oscillator

$$\vec{x}(\omega) = -\frac{e}{m}\frac{1}{\omega_0^2 - \omega^2 - i\omega\Gamma} \cdot \vec{E}(\omega). \tag{2.9}$$

Using the proportionality

$$\vec{p}(\omega) = -e\vec{x}(\omega) = \alpha(\omega)\vec{E}(\omega) \tag{2.10}$$

between the electric dipole moment, $\vec{p}$, and the electric field with the complex polarizability as the proportionality factor yields

$$\alpha = \frac{e^2}{m}\frac{1}{\omega_0^2 - \omega^2 - i\omega\Gamma}. \tag{2.11}$$

2.2.2 Optical dipole force

The optical dipole force on neutral atoms was initially postulated by Askar'yan in 1962 [11] and subsequently demonstrated by Bjorkholm et al. in 1978 [12].

The interaction between the induced dipole moment and the electric field results in a potential energy shift – known as the Autler-Townes effect or AC Stark shift. The interaction potential is given by

$$U(x, y, z) = -\frac{1}{2\epsilon_0 c}\mathrm{Re}(\alpha)I(x, y, z), \tag{2.12}$$

where ϵ_0 is the electric constant and I denotes the intensity of the light. The gradient of this potential,

$$\vec{F}(x, y, z) = -\nabla U(x, y, z) = \frac{1}{2\epsilon_0 c}\mathrm{Re}(\alpha)\nabla I(x, y, z), \tag{2.13}$$

is the dipole force.

2.2.3 Optical dipole trap

The optical dipole trap was proposed by Letokhov [13] and Ashkin [14, 15]. In 1986, the first optical trap for neutral atoms was realized by Chu et al. [16].

The dipole force can be used to create a potential well in which the atoms can be trapped. The conservative nature of the dipole force ensures that the energy of the trapped atoms is preserved, allowing for stable confinement within the potential well. To avoid atomic transition and thus heating, the wavelength of the light must be far detuned. Heating would lead to increased atomic motion which can cause the atoms to escape the trapping potential.

The wavelength of the light determines whether the trap is red- or blue-detuned. Red and blue detuning of the light refers to the frequency being below or above atomic resonance, respectively. For red-detuned light, atoms are attracted to regions of high intensity, congregating at the potential maxima. Conversely, atoms are repelled from regions of high intensity for blue-detuned light, congregating at the potential minima.

2.2.4 Trapping geometries

As outlined by Roy et al. [17], there are three main trap geometries of red-detuned traps. The first type is a focused beam trap which is formed by focusing a single beam with a Gaussian intensity distribution. The beam waist represents the spatial extent of the trapping potential. For a Gaussian beam following equation (2.2), the trapping potential is given by

$$U(x,y,z) = \frac{U_0}{1+\left(\frac{z}{z_0}\right)^2} \exp\left(-2\left(\frac{\rho}{w(z)}\right)^2\right). \tag{2.14}$$

The trap depth

$$U_0 = \frac{\alpha P}{\pi \epsilon_0 c w_0^2} \tag{2.15}$$

is proportional to the laser power P and the polarizability α. It reflects the potential energy barrier that confines the atoms within the trap.

The trap frequencies in the radial and axial directions are

$$\omega_\mathrm{r} = \frac{4U_0}{m w_0^2} \qquad \text{and} \qquad \omega_\mathrm{z} = \frac{2U_0}{m z_0^2}, \tag{2.16}$$

respectively. They refer to the oscillation frequencies of the atoms in the trap and determine its confinement strength. Higher trap frequencies correspond to stronger confinement of the atoms. The aspect ratio of the trap frequencies

$$\frac{\omega_\mathrm{r}}{\omega_\mathrm{z}} = \frac{\sqrt{2}\pi w_0}{\lambda} \tag{2.17}$$

proves that the resulting trap is anisotropic due to the radial intensity gradient providing tighter confinement than the axial gradient.

A second trap geometry is the crossed optical dipole trap which is formed by the intersection of two or more beams at an angle. The trapping potential for a trap consisting of a beam propagating in the z-direction and one in the x-direction is given by

$$U(x,y,z) = \frac{U_0}{1+\left(\frac{z}{z_0}\right)^2} \exp\left(-2\frac{x^2+y^2}{w(z)^2}\right) + \frac{U_0}{1+\left(\frac{x}{x_0}\right)^2} \exp\left(-2\frac{y^2+z^2}{w(x)^2}\right). \tag{2.18}$$

In the case of a crossed optical dipole trap, the trap depth is equal to $2U_0$ and the aspect ratio of the trapping frequencies is $\sqrt{2}$.

The third type is an optical lattice configuration. It is usually implemented by retro-reflecting a laser beam to create two counterpropagating waves of the same polarization.

The interference of these waves gives rise to a periodic potential, wherein atoms can be confined. The trapping potential for this trap geometry is

$$U(x,y,z) = \frac{4U_0}{1+\left(\frac{z}{z_0}\right)^2} \exp\left(-2\left(\frac{\rho}{w(z)}\right)^2\right) \cos^2(kz) \tag{2.19}$$

with a trap depth of $4U_0$ and a trapping frequency ratio of $\sqrt{2}\pi w_0/\lambda$.

The optical lattice can be expanded into more complex trapping geometries in two or three dimensions by the addition of laser beams.

Another important parameter is the periodicity or lattice spacing of the potential. In the case of two counterpropagating laser beams, the periodicity is equivalent to the node distance of the standing wave, which is equal to $\lambda/2$ for a laser wavelength of λ.

A generalization of the optical lattice is the use of waves that interfere at an angle instead of counterpropagating waves. This allows to dynamically alter the periodicity by modifying the angle of the standing wave, a concept that will be examined in greater detail in the subsequent chapter.

3 Accordion lattice

An accordion lattice is a one-dimensional optical lattice that allows for active control of the lattice spacing. The setup enables stable trapping of a cloud of atoms while continuously separating or compressing the atoms.

To create such a lattice, two parallel laser beams are focused by a convex lens and interfere at a shallow angle. As the lattice spacing of the interference pattern depends on this angle, the trap's periodicity can be tuned by changing the distance between the beams – as depicted in figure 3.1.

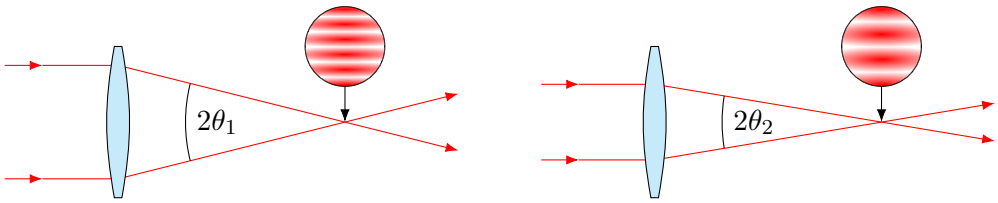

Figure 3.1: Beam paths at the final lens for different beam separations. Two parallel beams are focused by a convex lens, resulting in an optical lattice in the focal plane. For a smaller distance between the incoming beams (right image), the interference angle 2θ gets shallower, and the lattice spacing increases.

First implemented by Huckans in 2006 [5], traps for several ultracold quantum gases have been realized so far. In this thesis, a method to efficiently trap and squeeze atoms is presented, optimized to match the requirements of the experiment in terms of trapping frequencies, trap depth, and fringe size. The following section explains the steps and the most common methods used to create an accordion lattice setup.

3.1 Beam separation

First, a laser beam is split into into two parallel beams. In a commonly utilized method developed by Li et al. [18], a laser beam passes through a polarizing beamsplitter cube as shown in panel (a) of figure 3.2. The first beamsplitter reflects the s-polarized component of the incident beam, while allowing the p-polarized component to transmit through both beamsplitters unimpeded. A $\lambda/4$ waveplate converts the p-polarized component to circularly

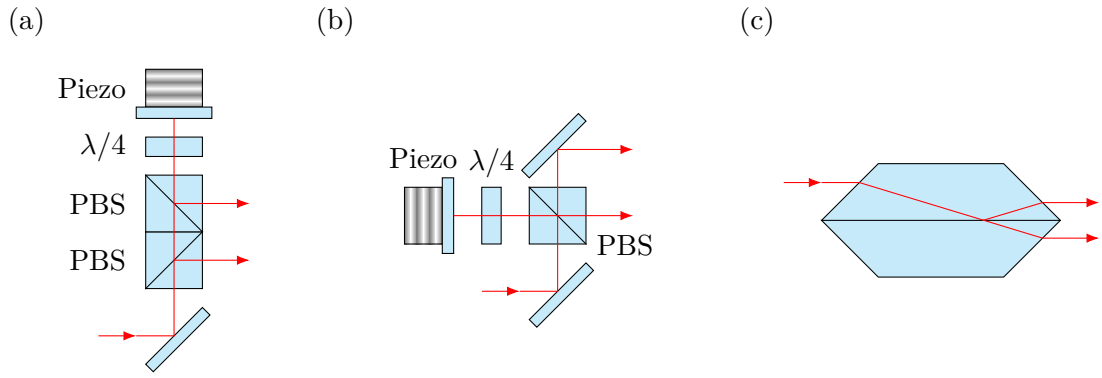

Figure 3.2: Schematic setups of different methods for beam separation. A common method (a) employs two polarizing beamsplitter cubes (PBS), which was simplified by substituting one beamsplitter with a mirror (b). A piezoelectric element enables active phase stabilization. An alternative approach (c) uses two Dove prisms that are adhesively bonded. Figure based on [19].

polarized light and the reflection at the mirror reverses the light's handedness. After the second pass through the waveplate, the light is converted to s-polarization and reflected by the upper beamsplitter, resulting in two parallel beams. This method has been implemented in several experiments [18, 20, 21].

As interferometric techniques are sensitive to phase differences, it is important to minimize the path difference of the two beams. A phase difference results in the central fringe being displaced from the center of the trapping potential, thereby causing it to move during compression and expansion. The movement of the lattice is transmitted to the atoms, which subsequently increases the temperature of the system and results in atom loss. The relatively large beam path difference inherent to this approach can be compensated for by extending one beam path with a set of mirrors [18].

In addition, the relative phase between the two beams must remain stable even when the lattice spacing is altered. Due to the movement of the incoming beam in this method, this condition is not fulfilled with the current approach. One solution to maintain a constant phase difference is to actively compensate for it with a piezoelectric element [19, 22]. As illustrated in figure 3.2, the piezo is attached to the back of the mirror. The phase shift is monitored and the optical path length is adjusted accordingly by applying a voltage to the piezo. Further information regarding the active phase stabilization can be found in reference [22].

A similar method, but with a reduced path difference from the start, was used by Kerkmann and Williams et al. [23, 24]. As shown in panel (b) of figure 3.2, one beamsplitter is replaced by a mirror. The p-polarized part of the laser beam is transmitted by the remain-

ing beamsplitter, the other part is reflected. Having undergone a change in polarization, it passes through the beamsplitter. It should be noted that this method also requires a piezo to compensate for the phase shift.

An alternative approach was implemented by the group of M. Greiner [25, 26]. Here, a custom beamsplitter intrinsically creates two parallel beams with equal path lengths, avoiding the need for active phase compensation. The beamsplitter is built out of two Dove prisms.

A Dove prism, named after H. W. Dove [27], is a prism whose base is an isosceles trapezoid with a 45° internal angle. A beam entering one of the sloped faces undergoes total internal reflection on the hypotenuse surface and emerges from the second sloped face. If the incident beam is parallel to the hypotenuse surface of the prism, it emerges parallel to itself.

For the accordion setup, two identical Dove prisms are aligned so that their hypotenuse surfaces touch each other; see panel (c) in figure 3.2. With a beamsplitter coating on one of the prism's hypotenuse surface, a beam entering one of the sloped faces is split into a reflected and a transmitted beam. Assuming a perfect alignment of the two prisms, a beam parallel to the beamsplitter surface will result in two parallel beams.

In contrast to the other methods, the Dove prism requires a demanding adjustment and gluing process with high requirements. However, there is no re-adjustment over time necessary because this only has to be done once. The rationale for adopting the Dove prism approach in this thesis is that it eliminates the necessity for active compensation of phase differences. There is no requirement to measure the phase for the feedback loop, which simplifies the final setup. Furthermore, this results in enhanced stability of the optical lattice and the avoidance of mechanical noise due to the piezo.

Figure 3.3 helps to geometrically derive a relation between the incoming beam position and the beam separation of the outgoing beams. Let x be the vertical distance between the point where the beam enters the prism to the beamsplitter surface of the two prisms. Analogously, y denotes the distance between the beam exit point and beamsplitter surface – which is half the beam separation for reasons of symmetry.

In the following calculations, dependencies of variables on the beamsplitter surface length l and refractive index n of the prisms are marked with indices. From the dotted right-angled triangle in figure 3.3, the relationship

$$\tan\left(\alpha_n + 45°\right) = \frac{l - x - y}{x + y} \tag{3.1}$$

follows. Solving for y and simplifying yields

$$y_{n,l}(x) = \frac{l - x - x \cdot \tan\left(\alpha_n + 45°\right)}{\tan\left(\alpha_n + 45°\right) + 1} = \frac{l}{\tan\left(\alpha_n + 45°\right) + 1} - x = \frac{l}{2}\left(1 - \tan\alpha_n\right) - x. \tag{3.2}$$

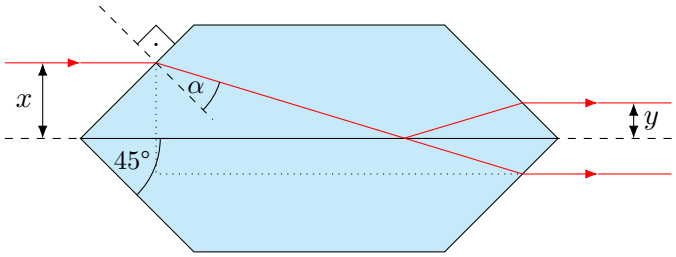

Figure 3.3: Side view of the Dove prisms showing the beam path. The laser beam hits the entry surface of the prisms at an angle of 45° and is refracted. At the coated beamsplitter surface, the beam is split into a transmitted and a reflected part. Both beams are again refracted at the exit surfaces, making them parallel. Figure drawn to scale.

To eliminate the angle α, Snell's law

$$n \sin \alpha = n_{\text{air}} \sin(45°) \quad \Rightarrow \quad \alpha_n = \arcsin\left(\frac{\sqrt{2}}{2n}\right) \tag{3.3}$$

with $n_{\text{air}} \approx 1$ is applied. Using $\tan(\arcsin u) = u/\sqrt{1-u^2}$, the final result

$$y_{n,l}(x) = \frac{l}{2}\left(1 - \tan\left(\arcsin\frac{\sqrt{2}}{2n}\right)\right) - x = \frac{l}{2}\left(1 - \frac{1}{\sqrt{2n^2-1}}\right) - x \tag{3.4}$$

shows that y is linear in x.

3.2 Beam displacement

A variation of the lattice periodicity can be achieved by altering the distance between the two beams that emerge from the beamsplitter. The presented methods for beam separation have in common that this distance can be altered by displacing the incoming beam. Various effective methods have been employed for this purpose.

The most straightforward method, as outlined by Li et al., is to mount the mirror ahead of the polarizing beamsplitter on a linear translation stage. In panels (a) and (b) of figure 3.2, this corresponds to a lateral movement of the lower mirror. For example, the distance between the beams is reduced when the mirror is shifted to the right.

For faster beam displacement, some groups replaced the translation stage with a rotating periscope [21, 26]. It consists of two parallel mirrors that can be rotated around the center. The periscope displaces the beam as a function of its angle via two reflections on the mirrors while maintaining the beam's original propagation direction. In comparison to a linear translation stage, this method significantly reduces the requisite time for shifting the beam, thereby enabling higher compression speeds of the lattice.

Another approach is to use an acousto-optic deflector (AOD) [24]. An AOD is a device that deflects a light beam by diffraction at an acoustic wave. AODs consist of electrodes which create a radio frequency drive signal with a variable frequency. This stimulates a piezo-electric transducer, exciting a longitudinal acoustic wave in an acousto-optic crystalline medium.

The acoustic wave can be understood as a periodic change in the refractive index. An incoming light beam is diffracted into multiple orders, as predicted by Brillouin in 1922 [28]. The diffraction angle depends on the sound wave periodicity, allowing for a precise control of the angle by changing the radio frequency.

For low frequencies, corresponding to the Raman-Nath regime, Raman-Nath scattering occurs (Debye-Sears effect). Differences in phase of the diffracted light lead to several orders with approximately equally intense beams. However, in AODs, the acousto-optical effect is used with the first-order beam as the output while the other orders are blocked. Therefore, this would lead to a low diffraction efficiency, which is defined as the ratio between first order and zeroth order intensity.

The diffraction efficiency can be improved greatly by using high frequencies in the range of several MHz, corresponding to the Bragg diffraction regime. For a laser beam incident at the Bragg angle, the refracted waves interfere constructively and most of the intensity will be in the first order.

However, the Bragg angle

$$\theta_{\mathrm{B}} = \frac{\lambda}{2n\Lambda} \tag{3.5}$$

depends not only on the optical wavelength λ and the refractive index n of the crystal, but also on the acoustic wavelength Λ. Therefore, it is not possible to satisfy the Bragg angle condition for all radio frequencies without realigning the input beam. Instead, the input angle is optimized for the center frequency with the consequence that the diffraction efficiency is reduced for the non-ideal input angles of other frequencies.

The change in diffraction efficiency with the frequency results in a characteristic, non-constant curve of laser power. Its broad maximum is interspersed by a dip, referred to as the mid-band degeneracy, which is a consequence of re-diffraction of the light. This gives rise to two important variables for characterizing an AOD: the deflection bandwidth and the center frequency. The center frequency indicates the center of the frequency range within which an AOD can operate most efficiently. It is intimately linked to the deflection bandwidth, which represents the width of the spectral range where the AOD's diffraction efficiency exceeds a certain threshold [29].

Besides the disadvantage of a fluctuating power output, this method is a very fast and precise solution for controlling the lattice spacing. The speed of compression when using an AOD is constrained by the acoustic velocity within the crystal as this determines the time required to update the radio frequency. Typically, this is on the order of a few microseconds, which is considerably faster than that of a translation or rotation stage. Furthermore, the AOD avoids mechanical vibrations and instabilities [24].

3.3 Interference

At this stage of the setup, the configuration creates two parallel beams with an adjustable distance between them. For the accordion lattice, the beams are focused down by a convex lens, subsequently referred to as the final lens. In the focal plane, the interfering light waves produce an interference pattern, which can be explained in the following way.

Depending on the vertical position of a point in the focal plane, the path length – and thus the phase – of the two waves differs. When the light waves are superimposed in accordance with the superposition principle, constructive and destructive interference occur depending on the relative phase. This can be observed as a variation in the brightness of the potential.

If the path difference is $\delta = k \cdot \lambda$ with $k \in \mathbb{Z}$, constructive interference takes place. The intensity maxima therefore appear at a distance of D, where

$$\sin\theta = \frac{\lambda}{2D}. \tag{3.6}$$

The angle between the beams is represented by 2θ and the laser wavelength by λ. In addition, the angle can be calculated as

$$\tan\theta = \frac{d}{2f}, \tag{3.7}$$

where f denotes the focal length of the final lens and d the distance between the two beams. Upon combining equations (3.6) and (3.7), the lattice spacing is

$$D = \frac{\lambda}{2\sin\left(\arctan\frac{d}{2f}\right)} = \lambda \cdot f \cdot \frac{\sqrt{\left(\frac{d}{2f}\right)^2 + 1}}{d} = \lambda \cdot \frac{\sqrt{\frac{d^2}{4} + f^2}}{d} \approx \lambda \cdot \frac{f}{d}. \tag{3.8}$$

For the approximation in the last transformation step, $f \gg d$ was assumed.

In what follows, the main steps to derive the intensity distribution in the focal plane will be explained. This derivation is based on the assumption that the two beams are circular, of equal power and waist size, and linearly polarized in x-direction. For a more comprehensive and detailed derivation, see [30].

The coordinates x, y, z have been defined such that the two beams are separated in the z-direction and initially propagate in the y-direction. The unit vectors are represented by $\hat{x}$, $\hat{y}$ and $\hat{z}$. The electric field vectors,

$$\vec{E}_{1,2}(x, y, z, t) = \hat{x} E_0 \cos(k_{1,2}\hat{y} \cdot \vec{x} - \omega t + \phi_{1,2}), \tag{3.9}$$

oscillate in time t with the angular velocity ω and have a constant amplitude E_0 and phase $\phi_{1,2}$. The final lens changes the propagation direction, resulting in the beam acquiring a z-component. The new wave vectors can be constructed by rotating the upper and lower beam by the angles $\pm\theta$ around the x-axis, respectively. Using the asymmetry of the sine function and the relationship between the wave number $k_{1,2}$ and the wavelength λ yields

$$k_{1,2}\hat{x} \mapsto \frac{2\pi}{\lambda} \cdot \begin{pmatrix} 0 \\ \cos\theta \\ \pm\sin\theta \end{pmatrix}. \tag{3.10}$$

To simplify the calculation, the complex representation of the electric field, denoted by $\vec{E}'$, with $\vec{E} = \operatorname{Re}\vec{E}'$, is introduced. In general, the intensity is given by the square value of the complex intensity. Due to the superposition principle, the electric fields can simply be added together and the final intensity distribution after interference is given by

$$I(x, y, z) = \left|\vec{E}_1' + \vec{E}_2'\right|.$$

Subsequent calculations lead to

$$I(x, y, z) = I_1 + I_2 + 2\sqrt{I_1 I_2}\cos\left(\frac{2\pi}{D}z + \Delta\phi\right). \tag{3.11}$$

The intensities of the individual beams, $I_{1,2}$, are similar to the intensity distribution represented by equation (2.2), which describes a Gaussian beam propagating in the y-direction. However, the coordinates must be rotated around the x-axis by substituting $y \mapsto \pm y\sin\theta + z\cos\theta$, resulting in

$$I_{1,2}(x, y, z) = \frac{2P}{\pi w(\pm y\sin\theta + z\cos\theta)^2}\exp\left(-2\frac{x^2 + (\pm y\sin\theta + z\cos\theta)^2}{w(\pm y\sin\theta + z\cos\theta)^2}\right) \tag{3.12}$$

Plugging this into equation (3.11) gives the final intensity distribution.

In the focal plane, where $y = 0$, the beams are identical:

$$I_{1,2}(x, y = 0, z) = \frac{2P}{\pi w(z\cos\theta)^2}\exp\left(-2\frac{x^2 + z^2\cos^2\theta}{w(z\cos\theta)^2}\right). \tag{3.13}$$

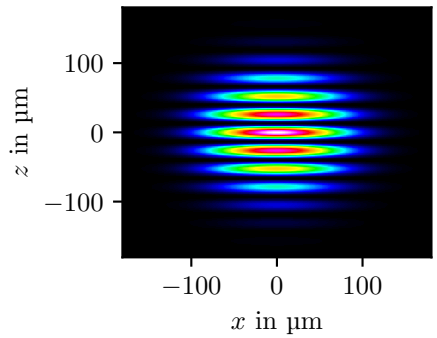

Figure 3.4: The theoretical intensity distribution in the focal plane of the final lens can be calculated using equation (3.14). The parameters are $w_0 = 100\,\mu\text{m}$, $R = \pi w_0^2/\lambda$, $\theta = 0.28$, $D = 26.50\,\mu\text{m}$, $\Delta\phi = 0$. They are chosen to match the later experimental values for a radio frequency of $f = 45\,\text{MHz}$.

Hence, the intensity distribution in the focal plane is given by

$$I(x, y = 0, z) = \frac{4P}{\pi w(z\cos\theta)^2} \cdot \exp\left(-2\frac{x^2 + z^2\cos^2\theta}{w(z\cos\theta)^2}\right) \cdot \left(1 + \cos\left(\frac{2\pi}{D}z + \Delta\phi\right)\right). \quad (3.14)$$

This equation is plotted in figure 3.4 for a specific set of parameters.

The Michelson contrast C is defined as

$$C = \frac{I_{\text{max}} - I_{\text{min}}}{I_{\text{max}} + I_{\text{min}}}, \quad (3.15)$$

where I_{max} and I_{min} are the maximum and minimum intensities, respectively [31]. For two beams of equal power, as derived in the calculation above, the contrast is $C = 1$. However, the contrast is reduced for two beams with non-equal intensities. If one beam has a relative power of P_{rel}, the contrast is given by

$$C(P_{\text{rel}}) = 2\sqrt{P_{\text{rel}}(1 - P_{\text{rel}})}. \quad (3.16)$$

As this function has the shape of a semi-circle and therefore a broad maximum around 50 %, the alignment is not sensitive with regards to unequal powers [26].

4 Experimental setup

In this chapter, the experimental implementation of an accordion lattice is described. The test setup uses a Fabry-Pérot laser diode (Thorlabs, `M9-A64-0200`) with a wavelength of 1064 nm and a power of 200 mW. As Fabry-Pérot lasers are edge-emitting laser diodes, the beam diverges at different angles parallel and perpendicular to the optical table. This results in an elliptical beam with a measured aspect ratio of 0.27. However, the accordion lattice necessitates a circularly symmetric beam profile with a Gaussian intensity distribution, so the beam must first be circularized.

4.1 Beam preparation

After the laser diode, a $\lambda/2$-waveplate and a polarizing beamsplitter linearly polarize the light, as shown in figure 4.1. The beamsplitter splits the laser beam into a p-polarized beam perpendicular to the incoming beam, which is blocked. The transmitted beam is s-polarized.

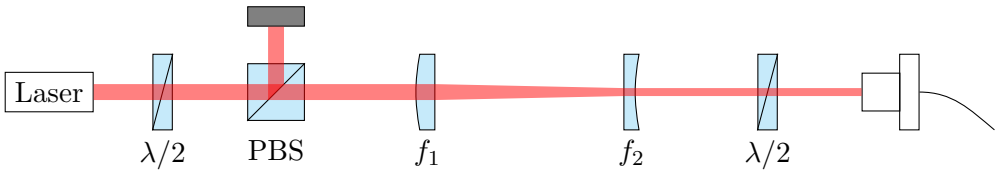

Figure 4.1: Schematic setup and beam path for beam circularization using a pair of cylindrical lenses. The light of a laser diode is linearly polarized by a $\lambda/2$ waveplate and a polarizing beamsplitter (PBS). While the reflected p-polarized part is blocked by a beamblock, the transmitted s-polarized part is circularized by a convex cylindrical lens with focal length $f_1 = 400\,\text{mm}$ and a concave lens with focal length $f_2 = -150\,\text{mm}$. Another $\lambda/2$-waveplate optimizes the polarization for the fiber coupler.

In order to shape the beam as circular as possible, a so-called anamorphic cylinder telescope is used. It consists of two cylindrical lenses with focal lengths $f_1 = 400\,\text{mm}$ and $f_2 = -150\,\text{mm}$; the distance between the lenses is chosen so that the lenses share a focal point. The beam profiles in figure 4.2 show that the circularization improves the ellipticity to 0.79.

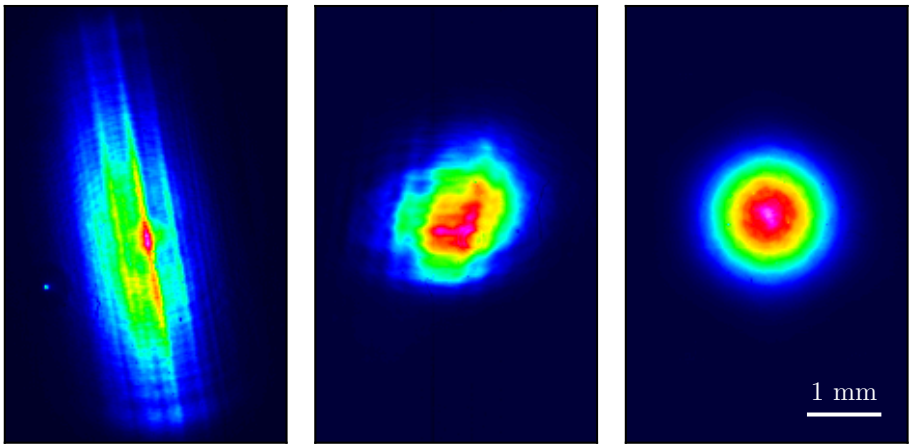

Figure 4.2: The beam profiles show the measured spatial intensity distribution at different points in the setup. The cylindrical telescope reduces the ellipticity from 0.27 (left image) prior to circularization to 0.79 (center). After the fiber (right), the beam is observed to be perfectly round with no discernible ellipticity, exhibiting a value of 1.00.

The easiest method to achieve a Gaussian intensity distribution is to utilize the beam-shaping property of a fiber. First, a $\lambda/2$ waveplate optimizes the polarization of the beam so that is aligns with the preferred input polarization of the fiber. This is done in order to minimize power fluctuations due to external perturbations such as thermal fluctuations. Subsequently, the beam is coupled into a polarization-maintaining photonic crystal fiber (NKT Photonics, `E324-443-200`). As depicted in figure 4.2, the beam is becoming circular and Gaussian to a good approximation.

The focal lens of the outcoupler (Schäfter + Kirchhoff, `60FC-SMA-T-23-A18-03`) is chosen to reach a final beam size for the accordion lattice of 1.98 mm. This beam diameter will be derived in section 4.5. Using a outcoupling lens with $f = 18.4\,\text{mm}$ and a fiber with a numerical aperture of $NA = 0.055$, the beam diameter d is expected to be

$$d = 2f \cdot NA = 2 \cdot 18.4\,\text{mm} \cdot 0.055 = 2.0\,\text{mm}.$$

Measurements confirm the beam size. As the beam must not diverge, it is collimated by adjusting the position of the lens in relation to the end of the fiber.

4.2 Lattice compression

Altering the lattice spacing in the accordion lattice requires changing the height of the beam prior to beam separation. This is achieved by modifying the first-order deflected beam of

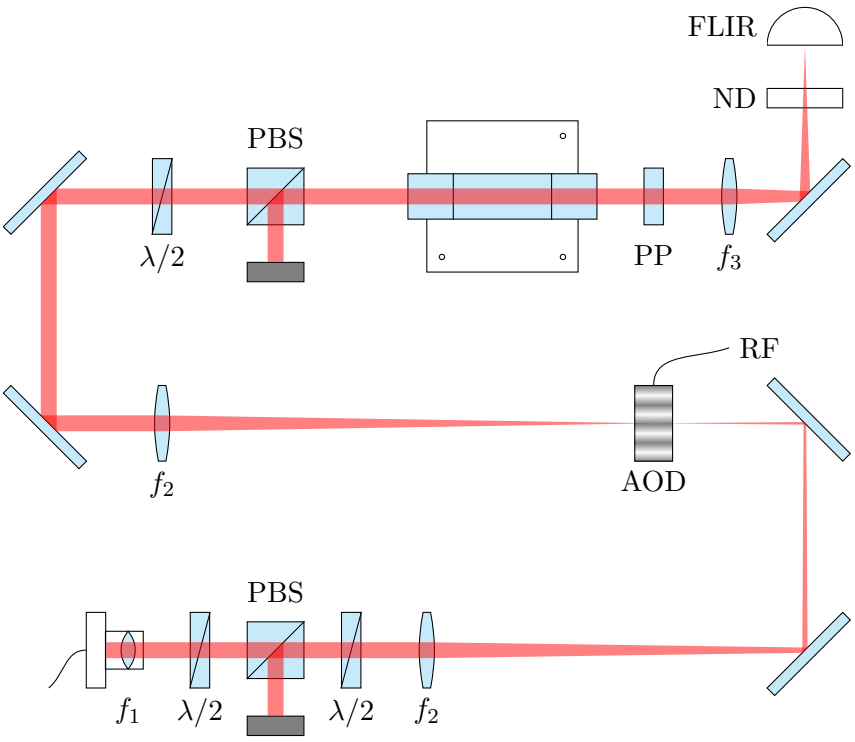

Figure 4.3: Schematic setup and beam path. The laser beam from the fiber coupler is collimated by a lens with a focal length of $f_1 = 18.4\,\text{mm}$. A waveplate and polarizing beamsplitter (PBS) are used to obtain a clean polarization. The polarization is rotated with another waveplate to match the preferred input polarization of the AOD, which deflects the beam depending on the applied radio frequency (RF). Two identical convex lenses with focal lengths of $f_2 = 500\,\text{mm}$ focus the beam into the AOD and collimate it again afterwards. After polarization state has been cleaned once more, the beam is separated by the Dove prisms. The relative phase of the two beams can be adjusted by rotating a phase plate (PP). The final lens with $f_3 = 293\,\text{mm}$ focuses the beam onto a FLIR camera. A neutral density filter (ND) prevents oversaturation.

an AOD (G&H, `AODF 4055-4`) through adjustment of the radio frequency.

The AOD has a preferred input polarization of 0° to the mounting plane. Therefore, the polarization state is cleaned with a $\lambda/2$ waveplate and a polarizing beamsplitter cube and then rotated by 90° with another $\lambda/2$ waveplate. This arrangement is visualized alongside the remaining setup in figure 4.3.

The laser beam is focused into the AOD using a lens with a focal length of $f_2 = 500\,\text{mm}$, chosen to minimize Bragg angle errors. The AOD then vertically diffracts the beam into multiple orders, with only the first-order beam utilized and the other orders blocked. For optimal diffraction efficiency, the AOD must be aligned with the incoming light at the Bragg

angle. This process yields a diffraction efficiency of up to 80 %.

As can be seen from the wiring diagram in figure 4.4, the AOD's electrical setup is as follows: a frequency generator produces a sinusoidal radio signal with an adjustable frequency, which is then amplified by a linear amplifier (Mini-Circuits `ZHL-1-2W-S+`) and sent to the AOD. As the AOD is manufactured for wavelengths up to 980 nm, the optimum radio frequency power for 1064 nm has to be found experimentally.

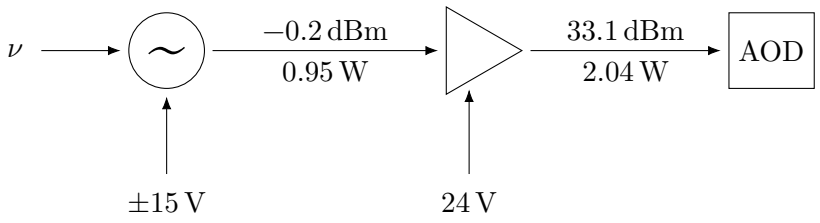

Figure 4.4: Wiring diagram of the AOD. The frequency generator produces a radio signal with an adjustable frequency, denoted as ν. An output power of $-0.2\,\mathrm{dBm} = 0.95\,\mathrm{W}$ has been selected, with the objective of achieving a power output of $33.1\,\mathrm{dBm} = 2.04\,\mathrm{W}$ following the amplifier. This value represents the optimal power setting which results in the most stable diffraction efficiency of the AOD for different frequencies. The voltages in the lower part of the diagram denote the power supplies for the frequency generator and amplifier.

As explained in section 3.2 and confirmed by the measured data shown in figure 4.5, the power fluctuates across the frequencies following a characteristic curve. It is possible to minimize the fluctuations by optimizing the radio frequency power, with the best stability at an input power for the AOD of approximately 2.05 W. This corresponds to 0.95 W before the amplifier.

For the desired lattice spacing, it is necessary to vary the distance of the outgoing beams between $2y = 4\,\mathrm{mm}$ and 36 mm. Using equation (3.4), the required change in height is determined to be 16 mm, corresponding to a frequency range of approximately 20 MHz. It can be observed that within the range between 30 MHz and 50 MHz, the power varies less than 30 %. Therefore, the center frequency employed for the purpose of aligning the setup is 40 MHz.

The deflection angle α is expected to change linearly with the radio frequency. To verify that this is the case, the vertical deflection δ is measured as a function of the frequency. The angle can then be calculated using $\tan\alpha = \frac{\delta}{f}$, where $f = 500\,\mathrm{mm}$ is the focal length of the lens after the AOD. As visualized in figure 4.6, the deflection angle does indeed increase linearly with frequency. Assuming the small-angle approximation, this implies a linear dependence in the vertical deflection as well.

Following the AOD, a second lens with the same focal length of $f_2 = 500\,\mathrm{mm}$ collimates

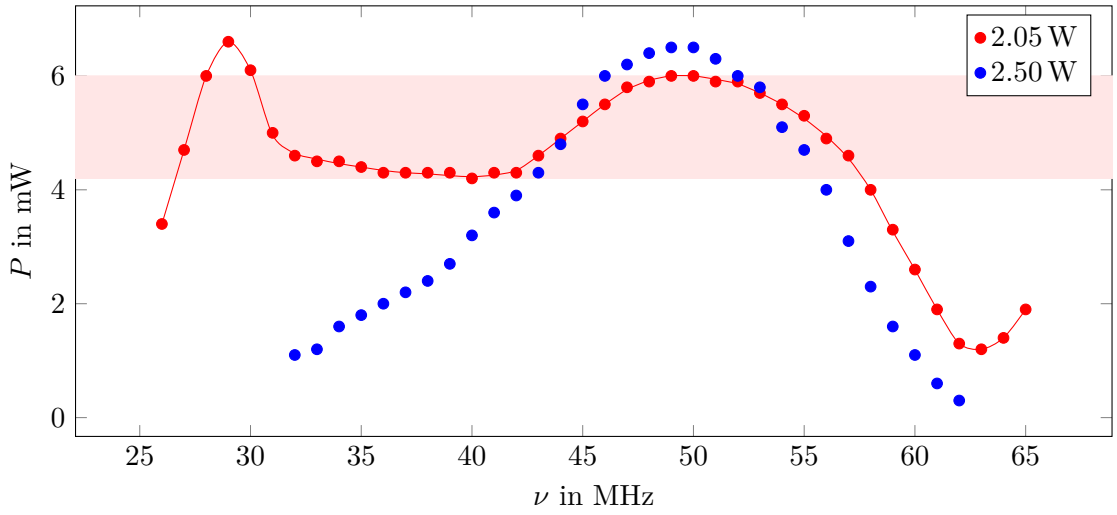

Figure 4.5: Measuring the power P of the first-order diffracted beam after the AOD for different radio frequencies ν gives a characteristic power curve with two distinct maxima. The regression curve (——) is derived from the measurement data (●). The optimal power stability is achieved at a radio frequency power of 2.05 W. Within the necessary frequency range, the power varies less than 30 %. For comparison, the bandwidth is significantly smaller for a radio frequency power of 2.50 W (●). Statistical errors are smaller than the size of the datapoint labels.

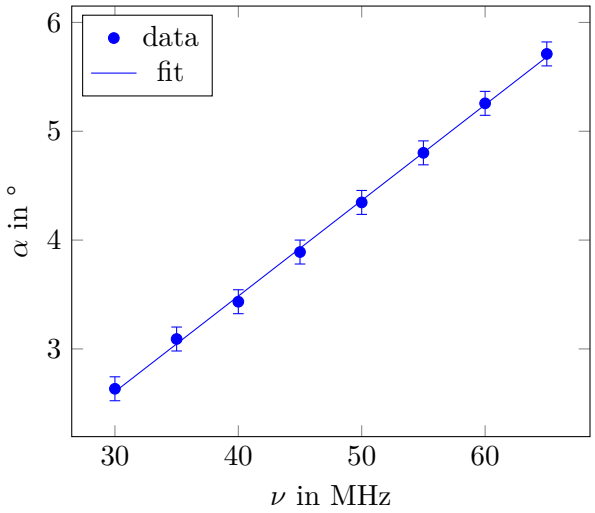

Figure 4.6: The plot of the diffraction angle α against the radio frequency ν shows a linear dependence. A linear fit function was used to determine the slope, which was found to be 0.0879 °/MHz. The error bars were calculated by error propagation based on a measurement accuracy of the vertical deflection of ±1 mm.

the beam. Using two identical lenses ensures that the beam size remains unaltered. The second lens must be oriented parallel to the crystalline medium of the AOD, in order to guarantee that the outgoing beams remain parallel to one another across the entire range of frequencies.

Given the risk of AOD-induced polarization disruption, a waveplate and polarizing beamsplitter cube clean the polarization again. The light is now s-polarized, which is the selected polarization for the beamsplitting process and the final trapping. The rationale for selecting s-polarization is to minimize Rayleigh scattering and subsequent heating of the system. The scattering rate is lowest if the laser polarization is perpendicular to the magnetic field direction [32]. As the magnetic field is oriented in the z-direction, the lowest scattering rate is expected if the electric field is aligned in the x-direction, which corresponds to s-polarization.

4.3 Alignment setup

To split the beam into two parts, two N-BK7 Dove prisms (Thorlabs `PS993`) with a refractive index of $n = 1.5066$ are used. The prisms must be precisely aligned relative to each other before being bonded together. Misalignments can lead to unequal path lengths or non-parallel beams. A custom alignment setup was designed and constructed from aluminum to achieve the required high accuracy.

The objective is to modify all degrees of freedom of the relative orientation in an independent and precise manner. There are six degrees of freedom, comprising three translational and three rotational degrees. The construction enables the adjustment of the upper prism in translation through the use of three translation stages (Opto4U `TS25`). Additionally, the lower prism can be modified in rotation through the integration of a rotation stage (Thorlabs `PR01/M`) and a custom-built tip-tilt stage.

Figure 4.7 illustrates the computer-aided design (CAD) model of the designed setup. As indicated in the CAD model and the photo of the assembled components in figure 4.8, the prisms are positioned in a U-shaped clamp and secured with four nylon screws per prism. The upper prism clamp is held in place by a mounting arm, whereas the lower prism is mounted on the tip-tilt stage, which is in turn attached on the rotation stage.

The design of the tip-tilt stage is inspired by mirror mounts and consists of a bottom and top plate [33]. These plates are connected with three vertical-drive adjusters on three of the corners and three tension springs in between. The tension springs are of an appropriate force to hold the plates securely in place and are hooked onto stainless steel rods, which are positioned within countersinkings.

To achieve optimal precision in alignment, screws with a very fine thread of 250 µm

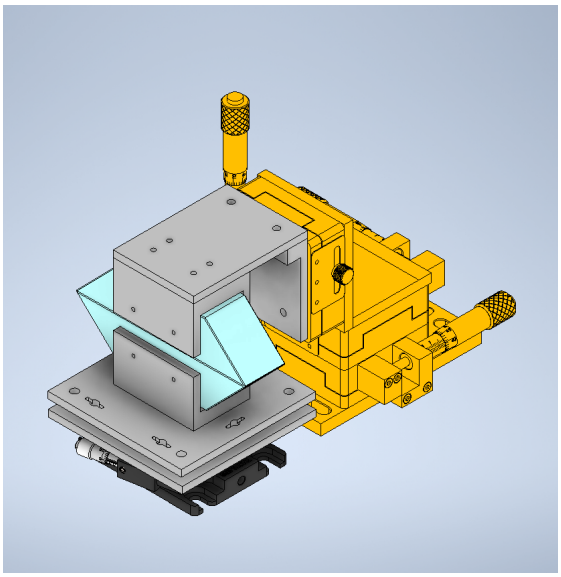

Figure 4.7: The CAD model of the setup illustrates the translation stages in orange, the prisms in blue, the custom-made parts in gray and the rotation stage in black.

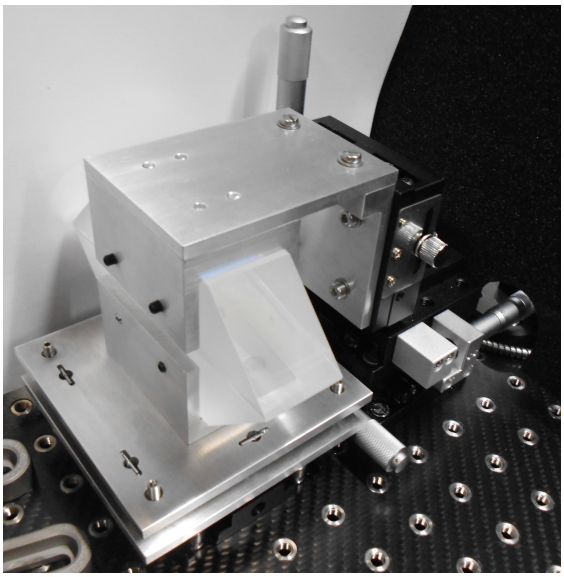

Figure 4.8: For comparison, this photo shows the manufactured and fully assembled setup.

per revolution are used. However, this is significantly finer than what is necessary for a stable thread in aluminum, making it susceptible to breakage. One solution that maintains accuracy while avoiding this issue is to use adjuster nuts with coarse external thread and fine internal thread.

As can be seen in figure 4.9, the bottom plate features a conical countersinking for the central screw and a slot for one of the other screws. The spherical tip of the screws allows them to glide within the countersinking or slot, preventing a shift of the plates parallel to each other.

The resulting precision with which the relative position can be adjusted is as exact as 0.5 mm per revolution in translation and 2.5° per revolution for rotation parallel to the optical table. For the rotation around both of the tip-tilt axes, the accuracy per revolution can be calculated via

$$\arctan\left(\frac{a}{b}\right) = \arctan\left(\frac{250\,\mu\text{m}}{80\,\text{mm}}\right) = 10.74'$$

from the screw pitch a and screw distance b.

One prism is coated on the hypotenuse surface with a beamsplitter coating in a 50 : 50 ratio, with the objective of achieving equal intensity for both beams. The beamsplitter

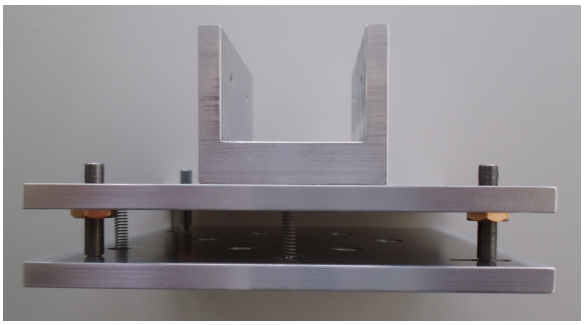

Figure 4.9: The custom-built tip-tilt stage consists of a lower plate and an upper plate. One of the prisms is mounted in a clamp, that is screwed to the top plate. Screw holes in three corners of the top plate allow to screw in bronze colored adjuster nuts. These have an internal thread of a fine gauge, designed to be used with fine-adjustment screws with a round tip. Two neighboring corners of the bottom plate feature a slot and a conical countersinking, respectively, to provide lateral support. Three tension springs are hooked onto stainless steel rods and hold the plates together. Holes in the lower plate allow for mounting the tip-tilt stage on a rotation stage.

coating is designed for s-polarization and an incident angle of

$$45^\circ + \alpha_n = 45^\circ + \arcsin\left(\frac{\sqrt{2}}{2n}\right) = 73^\circ;$$

This value is a direct consequence of equation (3.3).

Before applying any adhesives, the setup is tested using immersion oil (Bresser, `5912300`) with a refractive index of $n = 1.515$. This allows to become familiar with the adjustment process using a medium with a refractive index similar to that of the final adhesive.

4.4 Adhesive bonding

The Dove prisms are bonded together using an ultraviolet (UV) curing adhesive (Norland `NOA 61`). To achieve the necessary precision for aligning the prisms, a white light interferometer is used. Only if the path length difference is smaller than the coherence length of the light source, the white room light is dispersed into its spectral components. Since the coherence length of visible light is on the order of a few microns, this method provides a very accurate indication of the alignment.

First, the prisms are cleaned with isopropyl alcohol and an ultrasonic bath to remove any residual oil streaks. To prevent adhesive on the prism entrance and exit surfaces, as well as inside the clamp, the edges are masked with residue-free tape. The strips are left protruding to facilitate their removal at a later stage.

Once both prisms have been mounted in the clamps and any residual dust has been removed with compressed air, the adhesive is evenly distributed on the lower prism. The quantity of adhesive applied should be sufficient to cover the surface entirely, yet should not escape from the sides. A total of seven medium-sized drops was found to be an appropriate amount.

Then the mounting arm with the top prism is mounted and the stage is moved downwards at a slow and controlled rate until both prisms make contact with the adhesive. After the prisms have been aligned approximately, they are pressed together by lowering the stage to its lowest point. It is important to remove any excess adhesive immediately, to ensure that the adhesive is distributed uniformly across the entire contact surface, and that no air bubbles are trapped. The prisms should not be separated from now on, otherwise it will not be possible to bring them together without air inclusion.

To construct the interferometer, a two inch mirror coated for the visible spectrum is mounted in close proximity to the sloped faces of the prisms, as illustrated in figure 4.10. The tilt of the mirror is aligned by looking in y-direction through the prisms towards the mirror. Two slightly misaligned reflections can be observed if the mirror is not perpendicular to the hypotenuse surface of the prisms. By adjusting the top screw of the mirror, the reflections can be made to overlap, resulting in a single indistinguishable reflection. Given that rotating the mirror around the z-axis affects both paths equally, the remaining screw of the mirror is not essential for alignment.

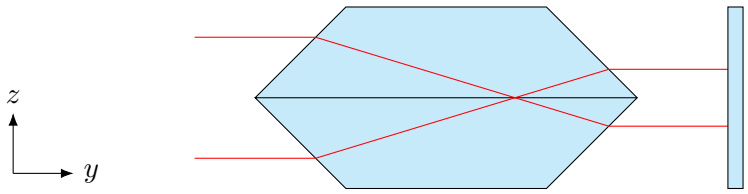

Figure 4.10: Light path in the white light interferometer for aligning the prisms. The spectral components of white light interfere constructively if both mirror and prisms are aligned so that the lengths of the upper und lower beam path are identical. Figure based on [25].

As a first step, the tip-tilt screws and translation stages of the prisms are adjusted by eye. The alignment process is to look down the axis of the beamsplitter and make incremental adjustments to all the screws until the desired interference pattern is visible. It is recommended that only two screws are adjusted at a time to systematically search for the optimal alignment. An initial indication of a good alignment is the emergence of a hatched pattern in an arbitrary orientation. Once interference is visible, the pattern is optimized for contrast and orientation with all screws, with the aim of achieving clearly visible, hori-

zontally oriented and broadly dispersed stripes. Figure 4.11 shows the observed white light fringes after the alignment process.

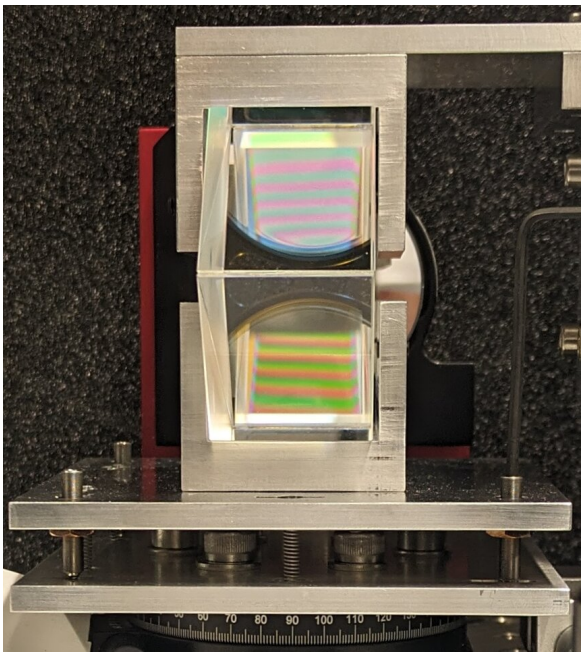

Figure 4.11: The aligned prisms display intense white light fringes, indicating that the beam paths are equal in the scale to the coherence length of the white light. The photo was taken along the axis of the beamsplitter surface with the mirror positioned behind the prisms for precise alignment using interference.

After all remaining tape strips have been removed, it is essential to ensure that no adhesive residue is present on any surfaces. If necessary, adjustments are made to ensure that the pattern is still clearly visible and in alignment.

The adhesive hardened significantly within approximately two to three hours due to the influence of naturally occurring UV light. Next, the expoxy is cured with a 4 W UV lamp from all sides for approximately 20 min. Subsequently, the UV lamp is mounted above the prisms and allowed to cure for several hours.

During the curing process, the interference pattern remained stable in position and orientation. However, there was a slight decrease in contrast. Once the adhesive bonding process is complete, the upper clamp, mounting arm, and translation stages are no longer required and can be disassembled.

4.5 Phase control and imaging

The beam emerging from the lower prism exhibits a phase shift due to reflection, resulting in unequal path lengths. To manipulate the relative phase between the two beams, a phase plate (Thorlabs, `BCP45R`) is positioned in the lower beam path in a way that allows for its rotation. Given the slower propagation speed of light in glass, this introduces a phase shift that depends on the rotation of the phase plate. As previously stated in section 3.1, the relative phase is responsible for determining the position of the central fringe and, thus, the stability of the interference pattern.

The two beams are focused by a fused silica plano-convex lens with a focal length of $f = 293\,\mathrm{mm}$ and an anti-reflection coating for 1064 nm light. The anticipated beam waist, $w_0 = 100\,\mu\mathrm{m}$, is achieved for a beam diameter of

$$d = \frac{2\lambda f}{\pi w_0} = 1.98\,\mathrm{mm},$$

as calculated using equation (2.5).

For imaging, a monochrome CMOS camera (FLIR, `BFS-U3-63S4M-C`) with a pixelsize of $2.4\,\mu\mathrm{m} \times 2.4\,\mu\mathrm{m}$ is used. The camera is placed on a stage which is adjusted so that the pixel plane of the camera is aligned with the focal plane of the final lens. In order to prevent oversaturation of the camera, a neutral density filter is placed in front of the camera.

5 Results

Figure 5.1 displays the experimentally determined interference pattern for a radio frequency of 45 MHz, alongside the theoretically predicted intensity distribution. In the measurement, an interference pattern with parallel stripes along the x-axis and a regular periodicity along the z-axis with an elliptical envelope is discernible. The observed patterns are simliar in shape and structure to the theoretically expected intensity distribution. However, the pattern is slightly noisy, which may be attributed to phase fluctuations and optical aberrations. Additionally, the minima appear less pronounced than in the predicted pattern. To gain further insight, the cross section of the pattern will be examined in the next section.

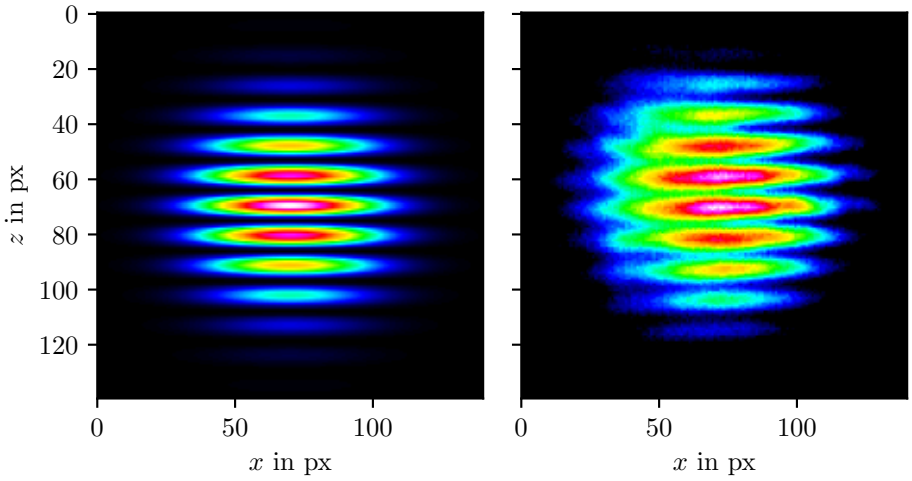

Figure 5.1: Comparison between the theoretically expected (left) and experimentally measured (right) intensity distributions for a frequency of 45 MHz. The expected plot is calculated using equation (3.14) for the case of two interfering beams that exhibit no phase shift. Also, the coordinates have been converted to pixels and shifted in order to ensure that both coordinate systems are aligned.

5.1 Cross section

The cross section in z-direction is obtained by extracting the intensity values of the central line of pixels from the intensity distribution in the focal plane. For a radio frequency of 45 MHz, the resulting cross section can be found in figure 5.2 alongside with the predicted curve. The predicted curve is calculated via equation (3.11) at $x = y = 0$. Here, the values of the parameters are $w_0 = 100\,\mu\text{m}$, $\theta = \arctan\left(\frac{14\,\text{mm}}{500\,\text{mm}}\right) = 0.028$, $D = 26.5\,\mu\text{m}$ and $\lambda = 1064\,\text{nm}$. The powers of the two beams and the position of the central fringe are obtained through a fit. While the shape generally matches the measured cross section, there are two notable differences. The first is that the cross section is asymmetrical, with greater intensity in the left half of the curve. This phenomenon can be fully explained by a phase difference between the two beams as the fit function in figure 5.2 with a variable phase demonstrates. Assuming a non-zero phase difference, the theoretical function is found to align closely with the observed measurements. The reason for the phase is that in this series of measurements, the phase plate was not properly aligned.

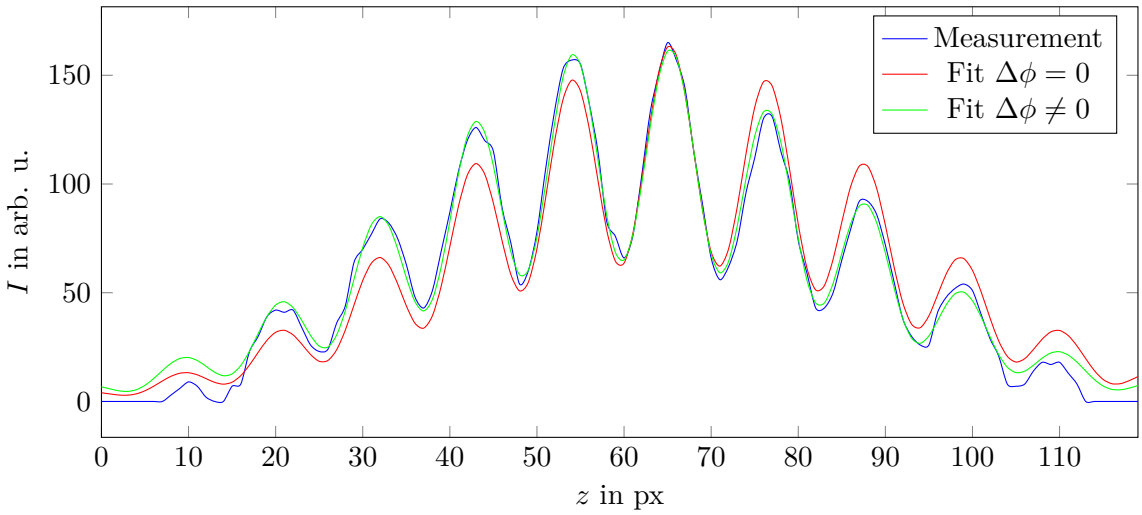

Figure 5.2: For a radio frequency of 45 Hz, the cross section is extracted from the intensity distribution in the focal plane (——). A fit function is included that follows the theoretical curve in equation (3.11) for $x = y = 0$ assuming no phase difference, i. e. $\Delta\phi = 0$ (——). While this initial fit generally aligns with the measured data, it fails to account for the asymmetry. Incorporating a phase difference between the two beams enhances the fit's accuracy; the fit function with $\Delta\phi \neq 0$ (——) closely aligns with the observed interference pattern.

5.2 Fringe contrast

A second notable discrepancy between the observed data and the theoretical model is the fringe contrast. Theoretically, the minima between the intensity maxima should have zero intensity. However, only a partial reduction in intensity is observed experimentally. The Michelson contrast is calculated from the highest maximum and minimum in the cross section via equation (3.16) for several frequencies. The graph in figure 5.3 shows that the contrast lies between 30 % and 50 % and increases with the radio frequency.

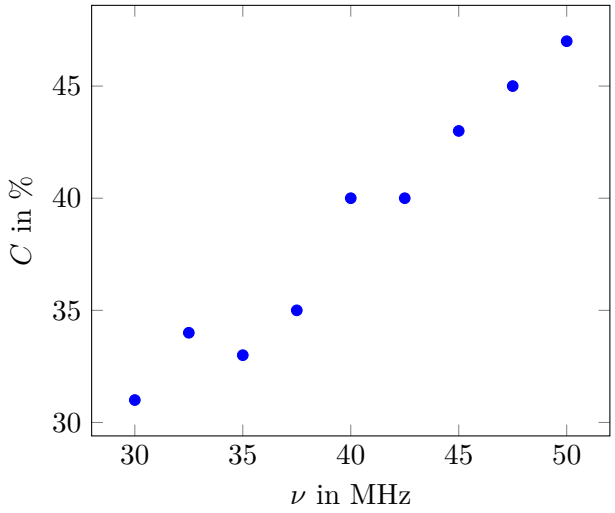

Figure 5.3: Contrast C of the interference patterns for several frequencies ν. It is calculated by extracting the maxima and minima from the cross section and substituting them into equation (3.16).

One contributing factor to the diminished contrast is the unequal power ratio between the two beams. Measurements confirm that the lower beam has a higher intensity than the upper beam, with a power ratio of 71 : 29. This suggests that the coating did not provide a perfect 50 : 50 power ratio, which is likely due to a wavelength shift during the coating process. For example, changes in the angle of incidence when the coating is applied to the surface can result in a shift of the coating's central wavelength. According to equation (3.16), the contrast is expected to reduce to

$$C = 2 \cdot \sqrt{0.71 \cdot 0.29} = 91\,\%.$$

Nevertheless, the fit parameters indicate a beam intensity splittage of 5 : 95, which is inconsistent with the observed results. To further investigate this phenomenon, a Michelson interferometer was set up after the outcoupler. Here, the contrast also did not exceed 50 %,

indicating that potential issues may already be present before the accordion lattice setup. It is plausible that these issues may be attributed to higher modes of the laser beam.

5.3 Stability during compression

The interference patterns for specific other frequencies are illustrated in figure 5.4; they also exhibit the anticipated characteristics. Both beams overlap precisely, with the exception of the lowest frequency. For 30 MHz the beams are slightly misaligned in the z-direction which is likely a consequence of spherical aberrations. It can be observed that the spacing increases for higher frequencies. This will be analyzed in more detail in the following section.

A crucial aspect of the accordion lattice is the stability of the central fringe. A shift in the interference pattern during compression or expansion will inevitably increase the velocity of the atoms and thus heat up the system. This shift is minimized by rotating the phase plate, which modifies the phase difference between the two beams. In the experiment, the central fringe remains at the same camera pixel within the necessary lattice spacing range from 30 MHz to 50 MHz. Therefore, the central fringe shift is less than $1\,\mathrm{px} = 2.4\,\mu\mathrm{m}$, which is equivalent to 0.3 waves of the pattern with the smallest periodicity.

5.4 Lattice periodicity

The periodicity of the lattice is determined by averaging the distances between neighboring maxima in the cross section. In addition to these values, the theoretical relation is also shown in figure 5.5.

The periodicity D as a function of the frequency ν is calculated using equation (3.8)

$$D(\nu) = \lambda \cdot \frac{f}{d(\nu)} = \lambda \cdot \frac{f}{2y(\nu)} \tag{5.1}$$

from the focal length of the final lens, $f = 293\,\mathrm{mm}$, and the vertical distance between the beam exit point and beamsplitter surface y. This distance can be calculated via equation (3.4)

$$y(\nu) = \frac{l}{2}\left(1 - \frac{1}{\sqrt{2n^2 - 1}}\right) - x(\nu) = 27.9\,\mathrm{mm} - x(\nu).$$

Here, $l = 126.3\,\mathrm{mm}$ is the length of the hypotenuse surface and $n = 1.4496$ is the refractive index of the prisms. The relation between x and ν is

$$x(\nu) = a + \sin(m) \cdot f_{\mathrm{AOD}} \cdot \nu, \tag{5.2}$$

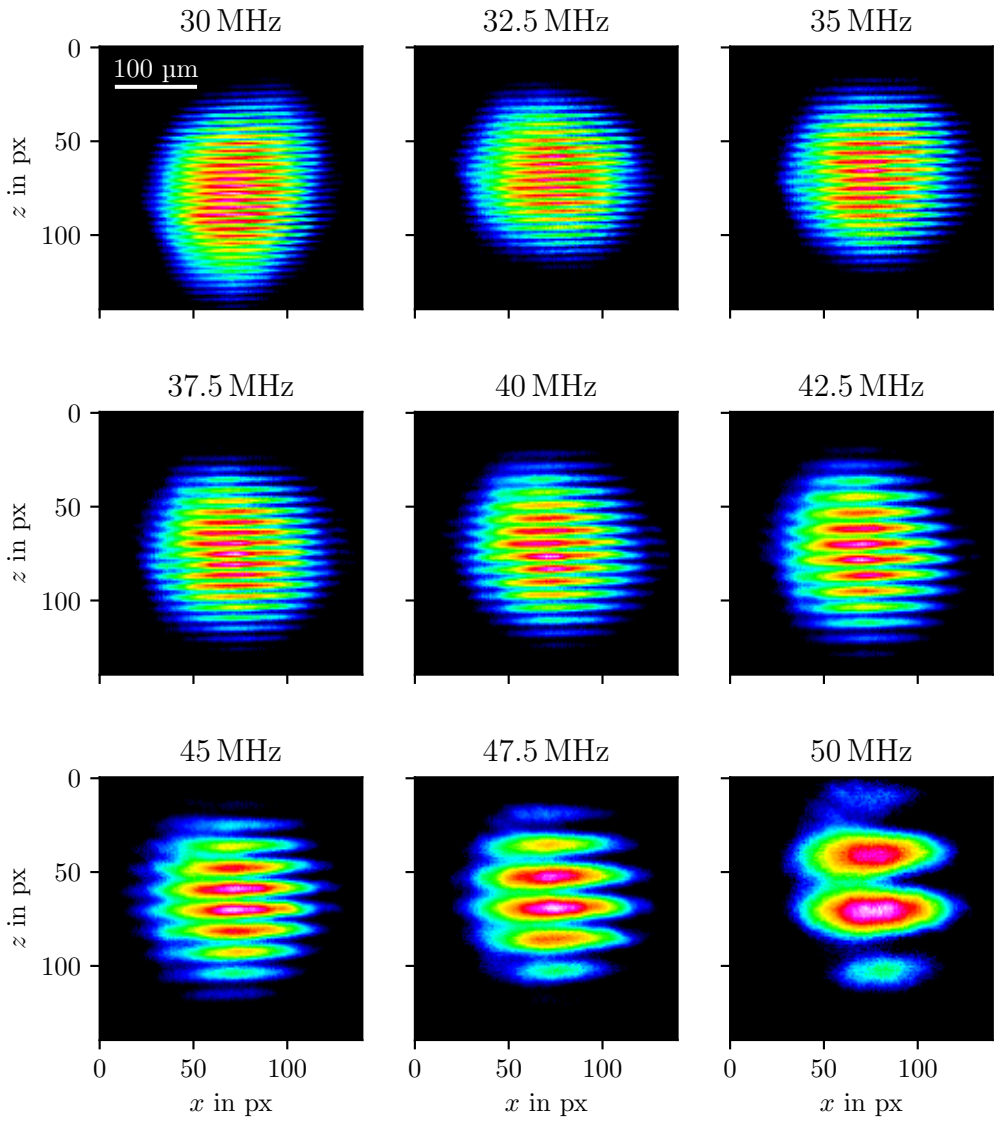

Figure 5.4: For different RF, the interference patterns in the focal plane of the final lens are measured by the camera. The intensity distributions are plotted as a function of the horizontal and vertical positions x and z, respectively, in units of pixels where $1\,\mathrm{px} = 2.4\,\mu\mathrm{m}$.

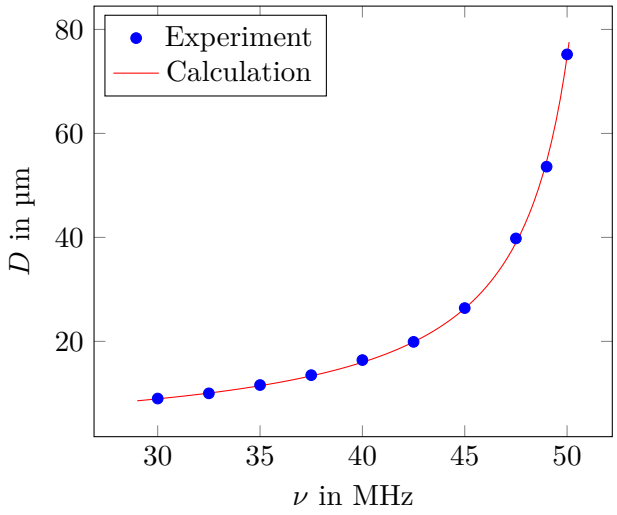

Figure 5.5: From the cross sections of the intensity profile in the focal plane, the average maxima distance D is determined for specific frequencies ν. Statistical errors are smaller than the size of the datapoint labels. The theoretical prediction is calculated using equation (5.3) and is in accordance with the experimentally determined values.

where $f_{\mathrm{AOD}} = 500\,\mathrm{mm}$. In this equation, $a = -12.5\,\mathrm{mm}$ describes the vertical offset between AOD and the hyperbolic surfaces of the prisms, and $m = 0.0879\,^{\circ}/\mathrm{MHz}$ is the slope determined in figure 4.6.

All relations collectively result in the concluding equation

$$D(\nu) = \frac{1064\,\mathrm{nm} \cdot 293\,\mathrm{mm}}{2\,(40.4\,\mathrm{mm} - 0.767\,\mathrm{mm/MHz} \cdot \nu)}. \tag{5.3}$$

As can be observed in figure 5.5, the measured periodicities align closely with the calculated curve. The maximum discrepancy between the observed data and the theoretical model is rather low at approximately 2 %. This enables the lattice spacing to be continously tuned over a range between 9 µm and 76 µm.

6 Conclusion and outlook

The experimental setup was successfully implemented and an accordion lattice with the requisite trap parameters was realized. This section provides a summary of the setup process and results, as well as an outlook.

After beam preparation, the laser beam is deflected using an AOD. A high diffraction efficiency of 80 % was achieved through optimizing the radio frequency power, the angle of the incoming laser beam as well as its polarization. The diffraction angle depends linear on the radio frequency. However, within the anticipated frequency range of 20 MHz, the power fluctuated significantly up to 30 %. To improve power stability, it is possible to utilize an AOD with a greater frequency bandwidth. Another potential solution is the implementation of a feed-forward control or an active feedback loop to regulate the radio frequency power dynamically [21].

The beam is divided into two parallel beams with intrinsically equal path lengths by a pair of Dove prisms. An alignment setup was constructed for the adhesive bonding of the prisms. The prisms were glued together using white light interferometry as a feedback mechanism for the alignment. The setup provided the necessary accuracy for adjusting the relative position of the prisms with great precision, as evidenced by white light fringes.

In the focal plane of the final lens, a monochrome camera images the intensity profile. An additional phase plate within one of the beam paths proved crucial for the stability of the central fringe, exhibiting a movement of less than 2.4 µm within the lattice spacing range. The limiting factor of the stability was not the setup itself, but rather the measurement to quantify the movement. If necessary, this can be easily improved by using a camera with a higher resolution or a telescope positioned in front of it.

The measured intensity distributions in the focal plane and the cross sections for different frequencies are found to be similar to the calculated predictions. The lattice spacing can be changed over a range between 9 µm and 76 µm in accordance with the theoretically expected values.

The low contrast between 30 % and 50 % represents an area for improvement. Although the precise cause remains undetermined, it is deemed unlikely that the accordion lattice setup is the source of the issue. This conclusion is based on measurements conducted with

a Michelson interferometer after the fiber outcoupler. As the contrast is relatively low to begin with, the observation suggests that the laser diode is a potential source of the problem. However, the contrast is expected to improve as the setup will transition to a different laser source with an output power of 15 W going into the accordion lattice setup.

The final setup will utilize fused silica prisms to avoid thermal lensing effects. Additionally, anti-reflection coating will be applied to the entrance and exit faces of the prisms. To enhance thermal stability, the setup will be enclosed by a housing to prevent fluctuations due to temperature shifts and airflow.

The next step in this experiment will be to test the setup with atoms. To achieve this, the test setup will need to be integrated with all the other optical lattice paths that are necessary to trap the atoms.

Bibliography

[1] I. Bloch, J. Dalibard, and W. Zwerger. “Many-body physics with ultracold gases”. In: *Rev. Mod. Phys.* 80.3 (2008), pp. 885–964.

[2] W. S. Bakr et al. “A quantum gas microscope for detecting single atoms in a Hubbard-regime optical lattice”. In: *Nature* 462.7269 (2009), pp. 74–77.

[3] M. Karski et al. “Imprinting patterns of neutral atoms in an optical lattice using magnetic resonance techniques”. In: *New J. Phys.* 12.6 (2010), p. 065027.

[4] J. Trautmann. “The Magnetic Quadrupole Transition in Neutral Strontium”. PhD thesis. Ludwig Maximilian University of Munich, 2022.

[5] J. H. Huckans. “Optical lattices and quantum degenerate rubidium-87 in reduced dimensions”. PhD thesis. University of Maryland, 2006.

[6] W. Demtröder. *Experimentalphysik 2. Elektrizität und Optik*. 7th ed. Springer Spektrum Berlin, Heidelberg, 2017.

[7] D. Meschede. *Gerthsen Physik*. 25th ed. Springer Spektrum Berlin, Heidelberg, 2015.

[8] E. Tiesinga et al. “CODATA recommended values of the fundamental physical constants: 2018”. In: *Rev. Mod. Phys.* 93.2 (2021).

[9] E. Hecht. *Optik*. 7th ed. De Gruyter, 2018.

[10] R. Grimm, M. Weidemüller, and Y. B. Ovchinnikov. “Optical Dipole Traps for Neutral Atoms”. In: *Adv. At. Mol. Opt. Phys.* Elsevier, 2000, pp. 95–170.

[11] G. A. Askar’yan. “Effects of the gradient of a strong electromagnetic beam on electrons and atoms”. In: *Zh. Eksp. i Teor. Fiz.* 42 (1962), p. 1672. [transl. in: *Sov. Phys. JETP* 15 (1962), p. 1088].

[12] J. E. Bjorkholm et al. “Observation of focusing of neutral atoms by the dipole forces of resonance-radiation pressure”. In: *Phys. Rev. Lett.* 41.20 (1978), pp. 1361–1364.

[13] V. S. Letokhov. “Narrowing of the Doppler width in a standing light wave”. In: *Pis’ma Zh. Eksp. Teor. Fiz.* 7 (1968), p. 348. [transl. in: *JETP Lett.* 7 (1968), p. 272].

[14] A. Ashkin. “Acceleration and trapping of particles by radiation pressure”. In: *Phys. Rev. Lett.* 24.4 (1970), pp. 156–159.

[15] A. Ashkin. “Trapping of atoms by resonance radiation pressure”. In: *Phys. Rev. Lett.* 40.12 (1978), pp. 729–732.

[16] S. Chu et al. “Experimental observation of optically trapped atoms”. In: *Phys. Rev. Lett.* 57.3 (1986), pp. 314–317.

[17] S. Roy, S. Chaudhuri, and C. Unnikrishnan. “Ultra-Cold atoms and Bose-Einstein condensates in Optical Dipole Traps”. In: *Laser and Bose-Einstein Condensation Physics*. Narosa Publishing House, 2010, p. 306.

[18] T. C. Li et al. “Real-time control of the periodicity of a standing wave: an optical accordion”. In: *Opt. Express* 16.8 (2008), p. 5465.

[19] V. S. Silva. “The Accordion Lattice: Towards Trapping of Dysprosium Ultracold Gases in Two Dimensions”. MA thesis. University of Heidelberg, 2023.

[20] D. Mitra et al. “Phase separation and pair condensation in a spin-imbalanced 2d fermi gas”. In: *Phys. Rev. Lett.* 117 (2016), p. 093601.

[21] S. Brandstetter. “Towards the Creation of Vortices in a Dipolar Bose-Einstein Condensate”. MA thesis. University of Innsbruck, 2020.

[22] C. Dietrich. “An accordion-type lattice: A tuneable dipole trap for ultracold gases”. MA thesis. University of Stuttgart, 2018.

[23] A. Kerkmann. “A novel Apparatus for Quantum Gas Microscopy of Lithium Atoms”. PhD thesis. Harvard University, 2021.

[24] R. A. Williams et al. “Dynamic optical lattices: two-dimensional rotating and accordion lattices for ultracold atoms”. In: *Opt. Express* 16.21 (2008), pp. 16977–16983.

[25] G. A. Phelps. “A dipolar quantum gas microscope”. PhD thesis. Harvard University, 2019. URL: `https://nrs.harvard.edu/urn-3:HUL.InstRepos:42029576`.

[26] A. Hébert. “A dipolar erbium quantum gas microscope”. PhD thesis. Harvard University, 2021. URL: `https://nrs.harvard.edu/urn-3:HUL.InstRepos:37368261`.

[27] H. W. Dove. “Das Reversionsprisma und seine Anwendung als terrestrisches Ocular und zum Messen von Winkeln”. In: *Ann. Phys.* 159.5 (1851), pp. 189–194.

[28] L. Brillouin. “Diffusion de la lumière et des rayons X par un corps transparent homogène: Influence de l’agitation thermique”. In: *Ann. Phys. (Paris)* 9.17 (1922), pp. 88–122.

[29] J. Eddie H. Young and S.-K. Yao. “Design considerations for acousto-optic devices”. In: *Proc. IEEE* 69.1 (1981), pp. 54–64.

[30] R.-J. Petzold. “Few ultracold fermions in a two-dimensional trap”. MA thesis. University of Heidelberg, 2020.

[31] A. A. Michelson. *Studies in Optics*. The University of Chicago Press, 1927.

[32] C. Bouazza. “Ultracold dysprosium gas in optical dipole traps : control of interactions between highly magnetic atoms”. PhD thesis. Paris Sciences et Lettres University, 2018. URL: `https://theses.hal.science/tel-01886206`.

[33] Private communication with G. Bisson, ETH Zurich.